Journal of Materials Chemistry A

PAPER

View Article Online
View Journal | View Issue

Cite this: J. Mater. Chem. A, 2019, 7, 12075

Degradation of $CH_3NH_3PbI_3$ perovskite materials by localized charges and its polarity dependency†

Min-cheol Kim,‡§[a] Namyoung Ahn,‡[a] Eunhak Lim,[b] Young Un Jin,[c] Peter V. Pikhitsa,[a] Jiyoung Heo,[d] Seong Keun Kim,[b] Hyun Suk Jung*[c] and Mansoo Choi*[ae]

Despite the excellent performance of organic–inorganic hybrid perovskite materials in recent years, the mechanism of their decomposition under actual operating conditions has not yet been elucidated. Herein, we elucidated the breakdown process of $CH_3NH_3PbI_3$ perovskite crystals and identified the polarity-dependent degradation pathway *via* localized charges by performing time-evolution measurements of the absorption spectra of perovskite films with different underlying charge transport layers and *ab initio* molecular dynamics calculations. It was found that the carrier polarity (hole-rich or electron-rich) inside the perovskite films played a critical role in the degradation rate, and the polarity-dependent degradation pathway strongly depended on the combination of the surrounding gaseous molecules. The hole-rich perovskite films degraded more rapidly than the electron-rich ones in the presence of H_2O, while this degradation trend was reversed in oxygen-only ambient environments. Interestingly, the hole-rich film is extremely unstable in atmospheric air containing both H_2O and O_2, whereas the $MAPbI_3$ film with excessive electrons was stable in air. An *ab initio* molecular dynamics simulation was performed to obtain the detailed degradation pathway of $MAPbI_3$ under atmospheric conditions for different polarities of the localized charge. The simulation results are in good agreement with experimental results, and the production of Pb(OH)I predicted in our simulations is confirmed by X-ray-assisted spectroscopic measurements.

Received 25th March 2019
Accepted 11th April 2019

DOI: 10.1039/c9ta03180d

rsc.li/materials-a

Introduction

A perovskite is an ionic crystal with three types of ions, in which the cation and anion are held together by electrostatic forces. As a perovskite material, organic–inorganic hybrid perovskites have recently attracted worldwide attention owing to their excellent performance in photovoltaics;[1–4] however, they have exhibited unstable characteristics when exposed to light and air.[5,6] As such hybrid perovskites have weaker hydrogen bonding between the organic cation and octahedral structure than between inorganic ones composing octahedral,[7] organic cations have been considered to be responsible for easy crystal de-bonding and chemical reactions with the atmosphere.[8,9] Hybrid perovskites change rapidly into inorganic halides after light-induced degradation.[10] Such fast decomposition of hybrid perovskites impedes the commercialization of perovskite-based photovoltaics.

The degradation of these perovskite materials has been studied in the past few years;[11–14] however, there remain several unknowns in and debates on the degradation mechanism because the process occurs in extremely complicated multi-molecular systems under real operating conditions.[10,15,16] As possible causes, researchers have previously suggested ion migration of a halide anion and the resulting deprotonation of an organic cation.[5,11,17,18] Furthermore, the role of gaseous molecules such as oxygen and moisture in perovskite material degradation has been researched extensively.[19–22] However, it is possible that the observed ion migration and deprotonation were merely a result of degradation and not the cause of degradation. Accordingly, determining the fundamental reason for the degradation is urgent for solving the stability issue.

We identified trapped charges in perovskite ionic crystals as the fundamental origin of perovskite material degradation under exposure to light illumination and the atmosphere.[23,24] We experimentally demonstrated that trapped charges accumulated along the grain boundaries and on grain surfaces induced irreversible degradation in the presence of water, oxygen, or air. We also performed an ab initio molecular dynamics (AIMD) simulation for $CH_3NH_3PbI_3$ ($MAPbI_3$) crystals

[a]Global Frontier Center for Multitscale Energy Systems, Seoul National University, Seoul, Republic of Korea. E-mail: mchoi@snu.ac.kr
[b]Department of Chemistry, Seoul National University, Seoul, Republic of Korea
[c]School of Advanced Materials Science & Engineering, Sungkyunkwan University, Suwon, Gyeonggi-do, Republic of Korea. E-mail: hsjung1@skku.edu
[d]Department of Green Chemical Engineering, Sangmyung University, Seoul, Republic of Korea
[e]Department of Mechanical Engineering, Seoul National University, Seoul, Republic of Korea

† Electronic supplementary information (ESI) available. See DOI: 10.1039/c9ta03180d

‡ These authors contributed equally to this work.

§ Present address: Department of NanoEngineering, University of California, San Diego, 9500 Gilman Drive, La Jolla, California 92093, USA.

with adsorbates of either H_2O or O_2 to examine whether the trapped charges could trigger the degradation of $MAPbI_3$. From these experiments and simulations, we determined the atomistic mechanism for the trapped-charge-driven degradation of $MAPbI_3$, in which trapped charges play a decisive role in breaking $MAPbI_3$ lattices owing to the intermolecular interaction with gaseous molecules under light soaking. However, whether the polarity of trapped charges could result in different pathways of the degradation of perovskite materials with the interaction with multi-molecular species under real operating conditions is still unknown.

In the present work, we elucidate the breakdown process of perovskite crystals caused by localized charges and its polarity-dependent characteristics through light-induced degradation experiments on $MAPbI_3$ perovskite films coated on different charge-selective layers.[25,26] The hole- and electron-rich $MAPbI_3$ layer can be realized in half devices, which are fabricated using the underlying charge-transporting layers. The existence of unbalanced hole and electron densities was evidenced by photoluminescence (PL), Kelvin probe force microscopy (KPFM) measurements, and theoretical calculations. These electron- or hole-rich half devices were exposed to different gaseous molecules under light illumination to determine the role of polarity-dependent localized charges on the degradation. In a moisture-only ambient environment, the degradation rate of the hole-rich $MAPbI_3$ film was much greater than that of the electron-rich one, while the oxygen-only case showed completely inverted results with respect to the degradation rates. More importantly, the actual atmospheric conditions (when oxygen exists with moisture) were highly aggressive only for the hole-rich $MAPbI_3$ film, whereas the electron-rich one was relatively stable (even more stable than in the oxygen-only case). Such interesting results suggest that there exists a direct correlation between polarity-dependent localized charges and degradation. To explain why and how the charge polarity influences the degradation rates depending on environments, we conducted AIMD simulations to study the intermolecular interactions between the $MAPbI_3$ components and gas mixture (oxygen and water) with different charge states (charge polarity of $MAPbI_3$). In the simulations, with a mixture of oxygen and water, it was found in the hole-rich case (with positive charge) that strong Pb–O bonding initially occurs, and this Pb–O bonding induces the vigorous destruction of the PbI_6 octahedron and finally produces hydroxide species owing to proton transfer from H_2O, which has been experimentally confirmed through X-ray-assisted spectroscopic measurements in the present study.

Results

Different degradation rates of $MAPbI_3$ depending on underlying transport layers

We employed perovskite films with different underlying layers to investigate the effect of the underlying layers on the degradation rates under light illumination and identical ambient conditions. We configured the half device with ITO/selective charge-extraction layer/$MAPbI_3$, in which the surfaces of the $MAPbI_3$ films were directly exposed to air without any passivation layer, and this configuration enabled films to be exposed to the same ambient conditions under light illumination. As discussed in detail in a later section, the half devices have unbalanced polarity of charge carriers in the $MAPbI_3$ films (owing to the selective charge-extraction, which results in unbalanced surface-localized charges that are confirmed by SKPM).[27] We performed degradation tests under different ambient conditions using our customized experimental setup in order to maintain a specific ambient condition inside the chamber (Fig. 1a). Interestingly, the degradation of the PEDOT:PSS/$MAPbI_3$ half device, which has excessive electrons, occurred much faster than that of the C_{60}/$MAPbI_3$ half device, which has excessive holes in a dry-air ambient environment (N_2(80%) + O_2(20%)) (Fig. 1b and c), while the humidified nitrogen ambient environment (N_2 + H_2O R.H. $\sim$ 80%) yielded totally inverted results, *i.e.*, in this case, the C_{60}/$MAPbI_3$ half device containing excessive holes was degraded much faster than the PEDOT:PSS/$MAPbI_3$ (Fig. 1d and e). Under 100% oxygen ambient conditions, the degradation occurred more rapidly than under dry-air ambient conditions, but exhibited the same trend depending on the underlying layers (ESI Fig. 1†). It should be noted that the PEDOT:PSS/$MAPbI_3$ half device exhibits very slow degradation in the humidified nitrogen ambient environment in contrast to the C_{60}/$MAPbI_3$ half device. When surrounded only by nitrogen, no light-induced degradation of the $MAPbI_3$ film was observed regardless of the underlying transport layers (ESI Fig. 2†), which is consistent with previous studies.[5,23] This means that the underlying transport layers cannot deteriorate the $MAPbI_3$ films even with unbalanced localized charges.

Previously, it was found that $MAPbI_3$ films could be decomposed under light illumination under dry air ambient conditions even without moisture.[5,11] This study demonstrated that superoxide (O_2^-) formed by the reaction of oxygen molecules with photo-generated electrons could degrade $MAPbI_3$ perovskites even in the absence of water molecules. We claim that, in the case of the TiO_2/$MAPbI_3$ half device, which can selectively quench electrons, the superoxide generation decreased as compared to the case of either the glass/$MAPbI_3$ or Al_2O_3/$MAPbI_3$ half device, which finally resulted in relatively slow degradation. Our experimental results also show similar results under dry air ambient conditions (Fig. 1b and c). However, the degradation rate under humidified nitrogen ambient conditions was completely reversed, which has not been observed before. These observations clearly show a strong dependency of the degradation rate on the type of underlying layers and surrounding ambient conditions. Obviously, a different charge transport layer changes the distribution of the charge-carrier polarity in the $MAPbI_3$ layer (explained below).

Unbalanced charge-carrier polarity in $MAPbI_3$ layers

The type of underlying layer influences the carrier density distributions in the $MAPbI_3$ layer under light illumination.[27] We prepared four different half devices to examine the change in carrier densities depending on the underlying layers *via* PL measurements. We used C_{60} (ref. 28) and $PC_{60}BM$[29] as electron

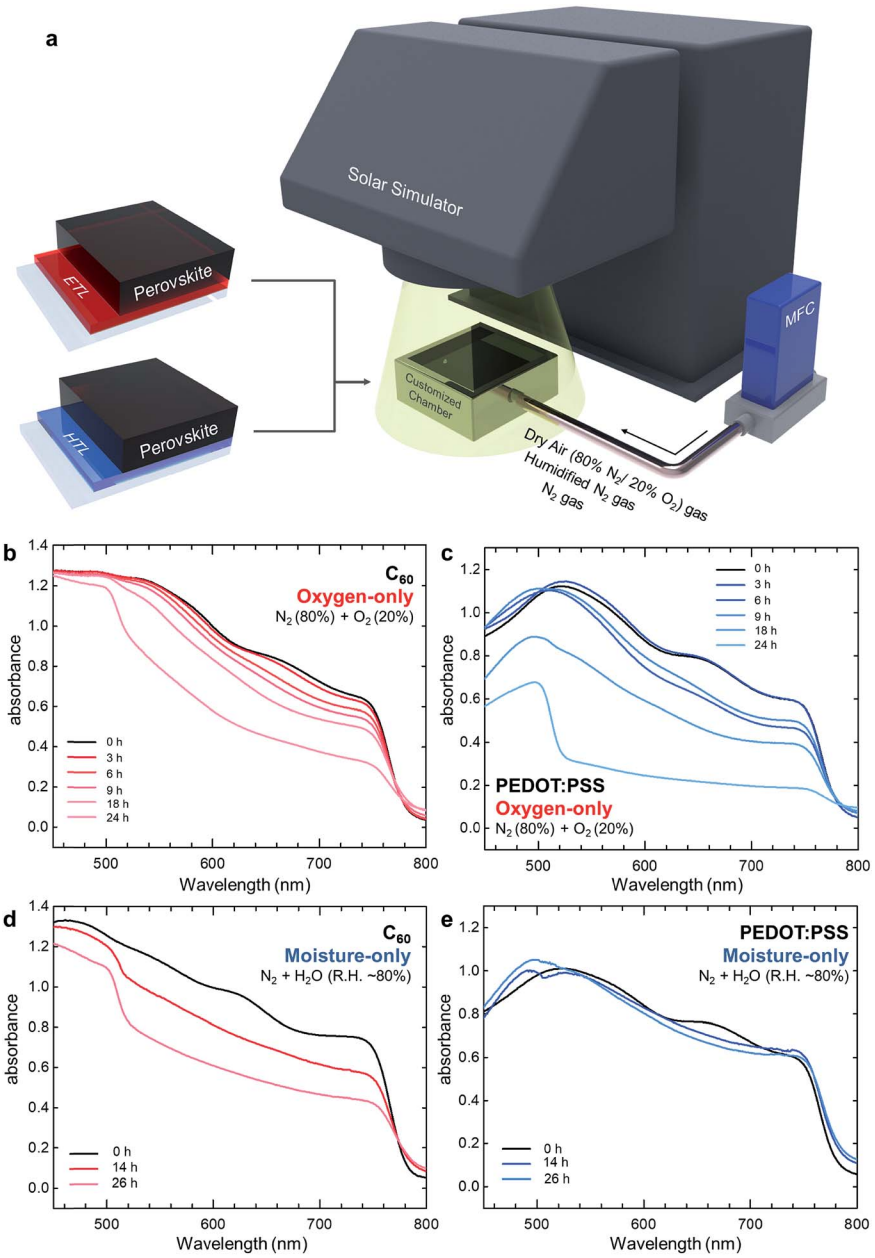

Fig. 1 Light-induced degradation test of perovskite films depending on the excessive charge polarity under different atmospheric conditions. (a) Schematic of customized experimental systems for light-induced degradation with a solar simulator, customized chamber and gas flow controller. Time evolution of absorption spectra for (b) the C_{60}/$MAPbI_3$ (hole-rich) and (c) the PEDOT:PSS/$MAPbI_3$ (electron-rich) half devices in a chamber filled with dry air (80% nitrogen and 20% oxygen). Time evolution of absorption spectra for (d) the C_{60}/$MAPbI_3$ and (e) the PEDOT:PSS/$MAPbI_3$ half devices in a chamber filled with nitrogen and water vapor (R.H. $\sim$ 80%). Every sample was kept under continuous light illumination except when measuring absorption spectra.

transport layers (ETLs), and PEDOT:PSS[30] and Spiro-MeOTAD[31] as hole transport layers (HTLs) for the half-device configurations. As the radiative recombination is proportional to the electron and hole densities,[32] the PL intensities are indicative of the carrier densities in the $MAPbI_3$ layers. Dramatic decreases in the PL intensities were observed in the case of either ETL/$MAPbI_3$ or HTL/$MAPbI_3$ half devices as compared to the case without transport layers, which indicates that photo-generated electrons and holes are selectively collected at the interface, respectively (ESI Fig. 3†). In the Spiro-MeOTAD case, additives such as 4-*tert*-butylpyridine (tBP) and bis(trifluoromethane) sulfonimide lithium salt (Li-TFSI) were not added in order to avoid the controversial issue regarding the effect of their corrosive properties.[33,34] Its charge-extraction property was not significantly influenced by the absence of additives, as indicated by the results of the PL measurements (ESI Fig. 4†). Similarly, time-resolved PL data also presented the strong carrier-extraction properties of ETL/$MAPbI_3$ and HTL/$MAPbI_3$ half devices (ESI Fig. 3†). The values of τ_1 (the fastest decay component) for these half devices, which correspond to the

charge injection,[35] were much smaller than those for the glass/$MAPbI_3$ film, as can be observed in ESI Table 1.† In other words, these results imply that such charge-selective layers strongly attract a particular carrier from $MAPbI_3$ films at the interfaces.

Based on the PL results, we can assume that the electron and hole densities at the interface are zero in the case of the ETL/$MAPbI_3$ and HTL/$MAPbI_3$ devices, respectively. By solving the carrier continuity equation while considering light absorption, carrier mobility, carrier recombination, carrier drift and diffusion, the electron and hole densities are obtained as a function of the thickness displacement under 1-sun illumination for different underlying layers (calculation details in the ESI†). Fig. 2c–e show the calculation results of the electron (n_e, indicated by the red line) and hole (n_h, indicated by the blue line) density distributions depending on the different underlying layers. The glass/$MAPbI_3$ device has uniform distributions owing to the absence of the charge selection layer, in which the orders of magnitude of the hole and electron densities are similar. A small difference originates from the mobility difference between the electron and hole.[36] In contrast, in the ETL/$MAPbI_3$ device, the hole densities are much higher than the electron densities owing to electron quenching at the ETL interface. Strong and fast electron transfer from $MAPbI_3$ to the ETL is inferred from the steep slope of the electron densities near the ETL interface. In contrast, the HTL/$MAPbI_3$ devices have inverted carrier distributions. In addition, it is not only confirmed that the hole densities change dramatically near the HTL interface in a manner similar to that in the ETL/$MAPbI_3$ case, but also that the electron density is greater than the hole density. It is clearly shown that the type of underlying layer results in an unbalanced carrier polarity (positive) in the $MAPbI_3$ film when photo-carriers are generated by light illumination. Moreover, we performed KPFM measurements.[37] The unbalanced carrier concentration in the $MAPbI_3$ layer can alter the quasi-Fermi level, as depicted in ESI Fig. 5,† which could correspondingly change the surface potential. Fig. 2f–h clearly show the different surface potentials depending on the underlying layer, which is in good agreement with the density distribution calculations. As the hole densities are much greater than the electron densities in the ETL/$MAPbI_3$ half device regardless of the thickness displacement, the device shows the highest potentials among the three types of half devices (Fig. 2i). Based on the trapped charge-driven degradation mechanism,[23] we can hypothesize that the different experimentally obtained degradation results for different charge selective layers can be attributed to the different charge polarities (electron-rich or hole-rich) in the $MAPbI_3$ films.

Correlation between degradation rates and charge polarity under different ambient conditions

In addition to the light-induced degradation of the half device configurations under the oxygen-only or humidified nitrogen-

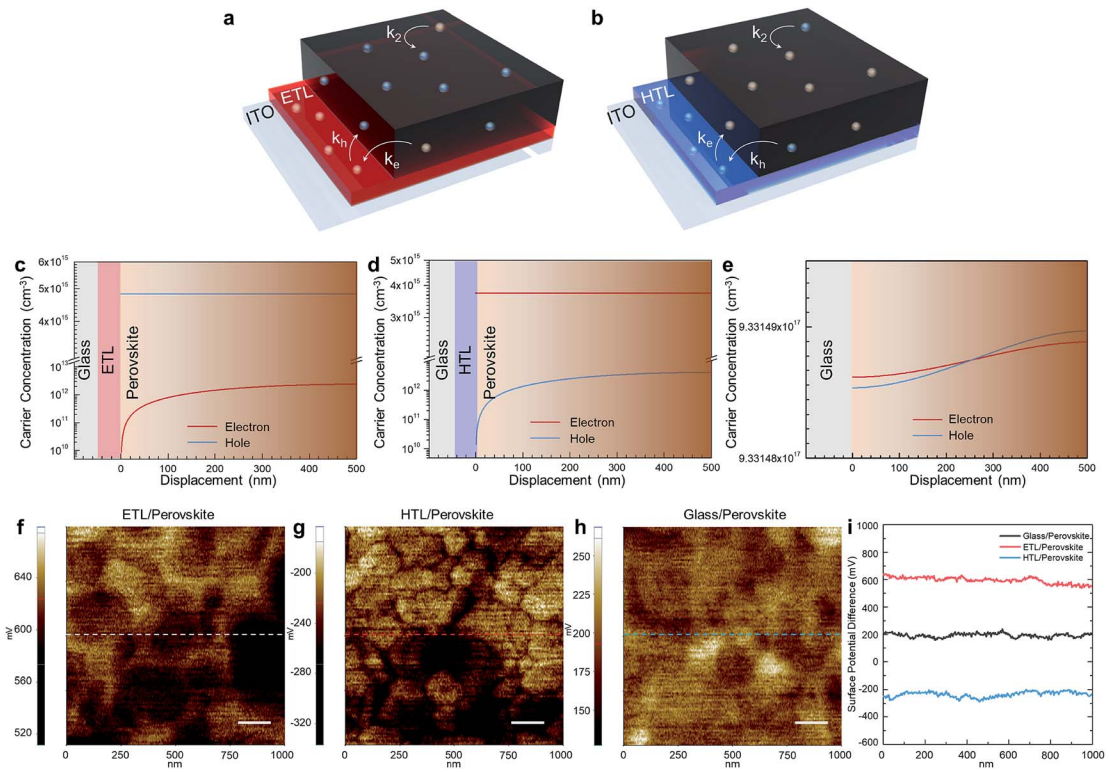

Fig. 2 Imbalance of charge polarity for charge-selective transporting half devices. Schematic of the experimental setup and charge-selective transporting half devices ((a) ETL/$MAPbI_3$ and (b) HTL/$MAPbI_3$ ones). Calculated carrier concentration as a function of thickness displacement for the $MAPbI_3$ film deposited on (c) glass/ETL, (d) glass/HTL and (e) the glass substrate. Surface potential energy distribution images measured by scanning Kelvin probe microscopy (SKPM) for the $MAPbI_3$ film deposited on (f) C_{60} (ETL), (g) PEDOT:PSS (HTL) and (h) the glass substrate. (i) Surface potential plot along the marked lines in (f–h), respectively. All the scale bars are 150 nm.

only conditions, we also performed degradation experiments under atmospheric air conditions with both oxygen and water (see Fig. 3a and b and ESI Fig. 6†). We observed unexpected outcomes in these experiments in terms of the degradation rates. The complete deterioration of the ETL/$MAPbI_3$ device occurred within 12 h, as shown in Fig. 3a. The degradation rates were much faster than those under either dry air or humidified nitrogen ambient conditions (see Fig. 3c). Furthermore, the mixture of oxygen and water violently destroyed the ETL/$MAPbI_3$ devices as compared to the case of oxygen-only or water-only ambient conditions. In contrast, the HTL/$MAPbI_3$ devices showed a surprisingly enhanced stability in humidified air, as observed in Fig. 3b. One remarkable observation in the case of HTL/$MAPbI_3$ is that the degradation in air with moisture occurred more slowly than the degradation in either air without moisture or humidified nitrogen without oxygen (Fig. 3d). Surprisingly, the addition of moisture improved the stability of the HTL/$MAPbI_3$ device. Analogous degradation trends were observed at any wavelength (550 nm, 650 nm and 750 nm) as can be seen in ESI Fig. 7.† Consequently, the mixture of oxygen and water results in extremely diametrical effects on the degradation rate depending on the type of underlying layer (different excessive carrier polarity). The origin of such different degradation rates is further studied at the atomic scale *via* AIMD simulations, the results of which are discussed below.

The X-ray diffraction (XRD) patterns for the pristine and illuminated $MAPbI_3$ films deposited on different charge transport layers support the observation (ESI Fig. 8†). The $MAPbI_3$ films with localized holes were characterized by the stronger intensities of their PbI_2 (100) peaks as compared to those with localized electron samples, which was in good agreement with the results of absorption studies. The observed change in the PbI_2 (100)/$MAPbI_3$ (110) peak intensity ratio before and after illumination is summarized in ESI Table 2.† The obtained SEM images demonstrate the same light stability trends that were observed during the absorption and XRD studies (ESI Fig. 9 and 10†). These results from the optical, spectroscopic, and morphological analysis indicate that gaseous molecules and their combination result in different degradation pathways depending on the localized charge polarity in $MAPbI_3$ crystals.

We also investigated the balanced charge-carrier density case by testing the $MAPbI_3$ film with no transporting layer (glass/$MAPbI_3$). In this case, the light-induced degradation occurred at a rate similar to that of the ETL/$MAPbI_3$, as shown in ESI Fig. 6.† Even if the $MAPbI_3$ had balanced carrier densities of electrons and holes, the magnitude of the carrier densities is much larger than that of the ETL or HTL/$MAPbI_3$ (Fig. 2c–e), which could induce faster degradation than that in the case of lower localized charges.

Discussion

Different degradation rates of $MAPbI_3$ under H_2O-only and O_2-only ambient conditions

It should be noted that the degradation rates of $MAPbI_3$ depend on the charge-carrier density and surrounding ambient

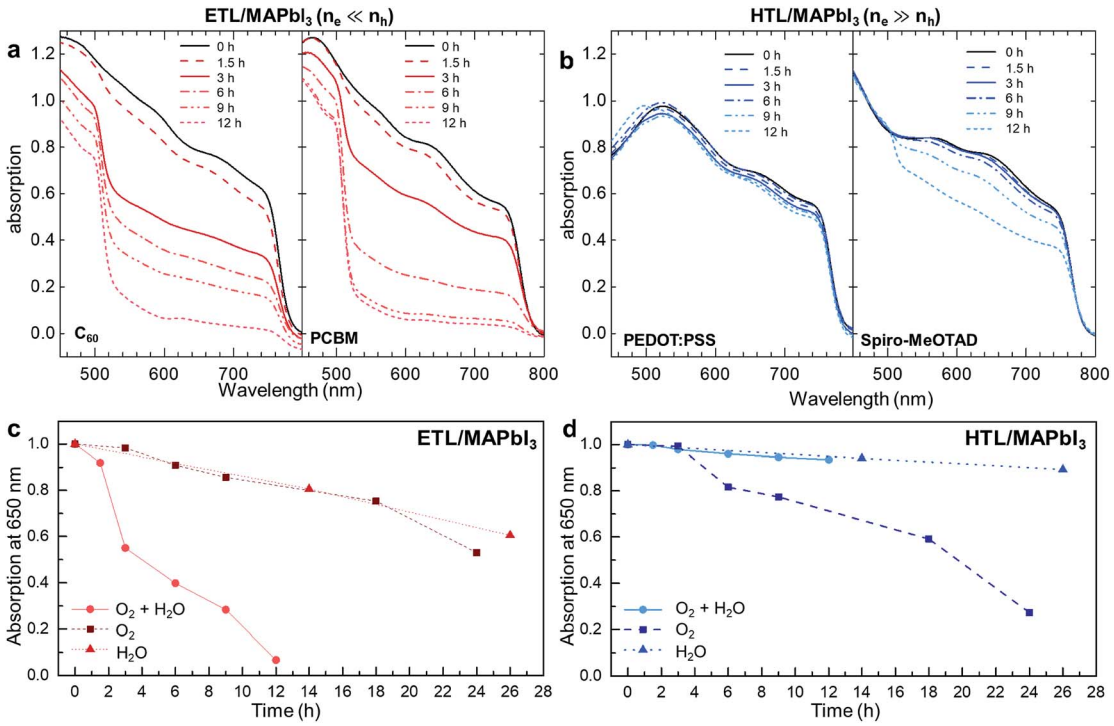

Fig. 3 Light-induced degradation in the mixture of ambient O_2 and H_2O depending on localized charge polarity. Time evolution of absorption spectra from 0 h to 12 h for (a) ETL/$MAPbI_3$ and (b) HTL/$MAPbI_3$ samples. C_{60} and PCBM were used for ETL/$MAPbI_3$ configuration and PEDOT:PSS and Spiro-MeOTAD for HTL/$MAPbI_3$ configuration. Time evolution of absorption spectra is summarized by plotting the absorption peak at 650 nm for (c) ETL/$MAPbI_3$ and (d) HTL/$MAPbI_3$ under 3 different ambient conditions (the ambient mixture, ambient O_2 (20%) and ambient H_2O (R.H. ~ 80%)).

environment to a great extent. We showed that the trapped-charge driven degradation mechanism is evidenced by experimental results and AIMD simulations in our previous studies.[23,24] As additional evidence for trapped-charge driven degradation, we discovered that the imbalance of the charge carrier (charge polarity) plays a different role in degradation rates in the present work. Based on the AIMD simulation results in our previous work,[24] we could determine how the charge polarity determines different degradation rates under H_2O-only and O_2-only ambient conditions. Most of the excess charges localized on the $MAPbI_3$ slab in the initial geometry. During the simulations, the charges were finally transferred to oxygen or water molecules, leading to different degradation pathways. According to the simulation results, the H_2O-only ambient environment shows different solvation characteristics depending on the polarity of $MAPbI_3$ crystals.[24] Water molecules solvate methylammonium cations (MA^+) at the surface of the $MAPbI_3$ crystal with localized holes (positive polarity), while in the case of a negative polarity, water molecules surround and solvate the iodide anions (I^-) and form hydrogen bonds (HI). As hydrogen bonding between MA^+ and PbI_6^- is weaker than the covalent bonding between Pb and I in the PbI_6 octahedron, MA^+ could be more easily solvated by water owing to such a weak bond strength. As a result, the $MAPbI_3$ crystals with localized holes became unstable in the moisture-only case owing to the easy solvation of MA^+. The relatively heavy I^- anions with strong bonding are more durable against water solvation in the case of $MAPbI_3$ with a negative polarity. These observations are in good agreement with our present experimental results of the moisture-only degradation test (Fig. 1d and e). In the oxygen-only case, $MAPbI_3$ crystals with a negative polarity were broken down faster than the ones with localized holes, which was attributed to highly reactive superoxide generation. In our previous AIMD simulation results,[24] the generated superoxide formed Pb–O bonding, thereby breaking down the PbI_6^- octahedron. Different quantities of generated superoxide depending on the charge polarity were obtained in these simulation results. The $MAPbI_3$ crystals with a negative polarity generate more superoxides than those in the positive polarity case, which is consistent with the results reported by Haque *et al.*[5,11] The difference in the degradation rates from our experimental results under oxygen-only ambient conditions (Fig. 1b and c) can be clearly explained by the difference in the quantity of superoxide generated.

AIMD simulations for $MAPbI_3$ breakdown in a mixture of O_2 and H_2O

We observed completely different degradation behavior in the presence of both oxygen and water (Fig. 3a and b), the reason for which is yet to be determined. A completely different degradation behavior in the combination of oxygen and water indicates that there exist distinct and complicated intermolecular reactions depending on the charge polarity of the $MAPbI_3$ crystals. Therefore, it is of great importance to investigate the mechanism of the degradation of $MAPbI_3$ under real operating conditions comprising both oxygen and water. In order to explore the intermolecular dynamics of oxygen and water depending on the polarity of the localized charges, AIMD simulations with a configuration containing both oxygen and water molecules were performed for the first time. We set an initial geometry with two rigidly fixed $MAPbI_3$ units at the bottom, two relaxed $MAPbI_3$ units at the top to form the surface, and embedded oxygen and water molecules into the gaps between the atoms. The surfaces of the $MAPbI_3$ crystals are terminated by MA cations and I anions and given different net charges (+1, 0, or −1) in the unit cell to model the localized charges. Fig. 4a–c present the molecular dynamics of $MAPbI_3$ crystals with the surrounding single oxygen molecule and three water molecules depending on the charge state (+1, 0, or −1). Interestingly, in the case of a +1 charge, the PbI_6^- octahedron at the surface is easily destroyed, while other charge states present a stable octahedral structure of PbI_6^- with the same surrounding molecules (see ESI Video 1† for detailed information). To check the effect of the initial configurations of molecules, we additionally studied different initial geometries ($2H_2O$ and $1O_2$) as shown in ESI Fig. 11.† Both simulation results are in agreement with those of the present experiment that shows the fast degradation of the hole-rich half device in the mixture of water and O_2. The destruction of the PbI_6 octahedral structure in the +1-charge state can be attributed mainly to the formation of a strong Pb–O bond, which was not observed in the neutral and −1-charge states. Furthermore, after the Pb–O bond generation, a domino effect of proton transfer from the surrounding water molecules finally results in the deprotonation of the MA^+ cations, which are turned into methylamine gases (750 fs in Fig. 4a). Such molecular dynamics in the +1-charge state would explain why the fastest degradation of the ETL/$MAPbI_3$ device ($MAPbI_3$ with localized holes) was observed in humidified air. In the neutral charge state, the oxygen molecules gradually drift apart from the $MAPbI_3$ surface, and the water molecules do not react with any $MAPbI_3$ components (see Fig. 4b and ESI Video 2†). This again confirms the trapped-charge-driven degradation in which the degradation of the perovskite materials occurs only in the case of the existence of trapped charges. Furthermore, the −1-charge state results in interesting molecular interactions, in that an oxygen molecule attaches to an iodide anion, but there is no further destruction of the PbI_6^- octahedron (Fig. 4c and ESI Video 3†), which indicates that the oxygen could not directly attack the Pb atom at the center of the PbI_6 octahedron in the $MAPbI_3$ crystals with the localized electrons.

To clearly compare the intermolecular interactions in these systems, we analyzed the Pb–O, I–O, and O–H distances for atoms of interest during the simulation, respectively (Fig. 4d–f). In the +1-charge state, the Pb and I atoms of the $MAPbI_3$ crystal have the strongest interactions with oxygen molecules, which is evidenced by the shortest Pb–O and I–O distance in Fig. 4d and e. In contrast, there seems to be a weak intermolecular interaction between the $MAPbI_3$ components and gaseous molecules in the case of both the neutral and −1-charge states (Fig. 4d–f). Furthermore, we compared the O–H distance to verify the deprotonation of the MA^+ cation. The hydrogen and oxygen atoms are components of the MA^+ cation and water molecules,

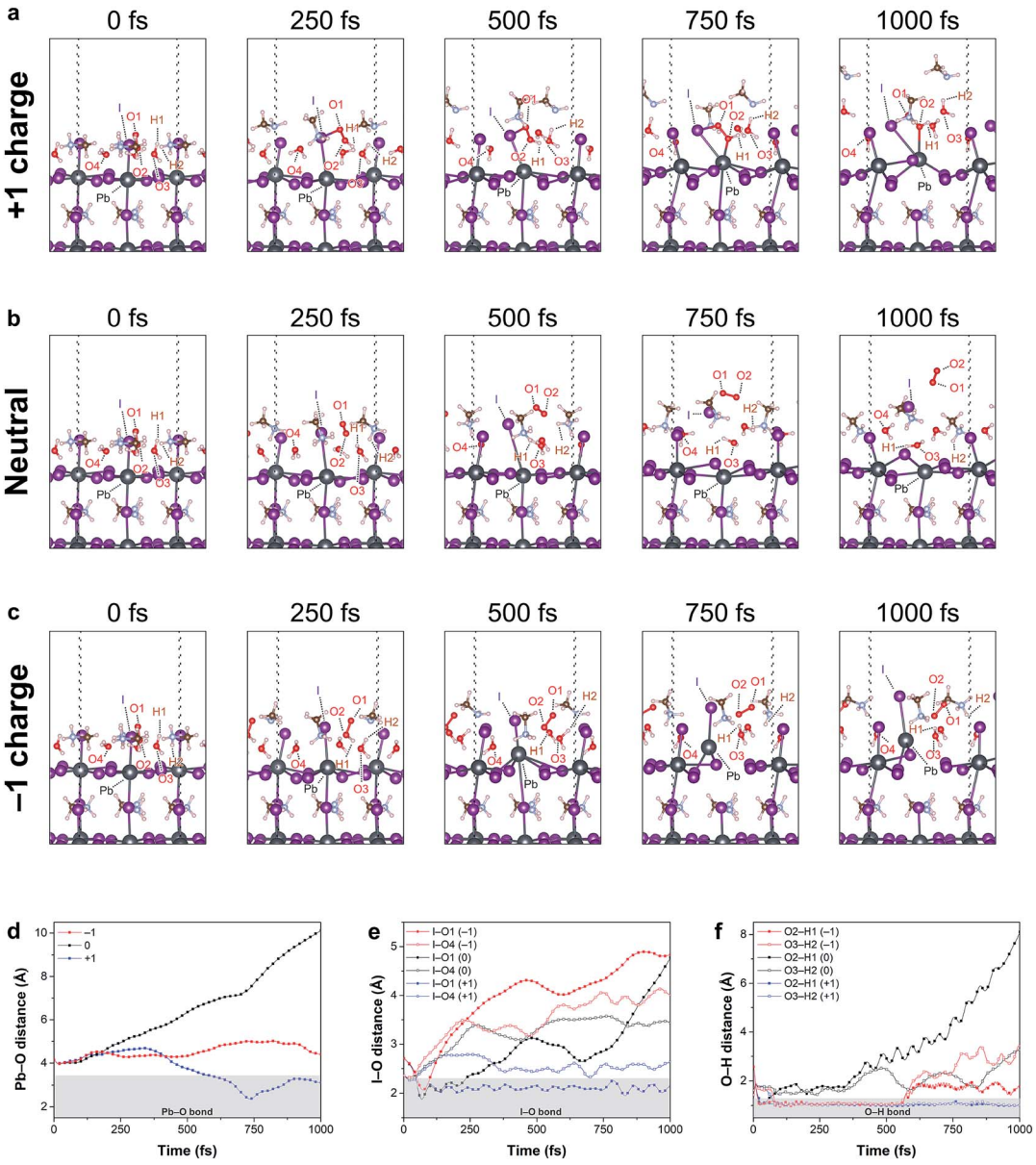

Fig. 4 Atomic scale investigation on molecular dynamics by AIMD simulation. Time evolution of molecular dynamics simulations of the $MAPbI_3$ surface for (a) +1 unit charge (one localized hole), (b) neutral, (c) −1 unit charge (one localized electron) under a $3H_2O$ and $1O_2$ ambient atmosphere. Tracking of atomic bonding distance of (d) Pb–O, (e) I–O and (f) O–H bonds for 1 ps, respectively.

respectively. The shortened O–H distance of 1 Å directly indicates the deprotonation of the MA^+ cation, which is only observed in the +1-charge state and not in the other states (see Fig. 4f). Overall, the intermolecular interactions between the $MAPbI_3$ components and gaseous molecules actively take place when the $MAPbI_3$ crystals are in the presence of localized holes, which clearly explains the experimentally observed fastest degradation of $MAPbI_3$ with localized holes.

Possible scenario of breakdown of $MAPbI_3$ crystals in the mixture of O_2 and H_2O

Based on the experimental results and AIMD simulations, we suggest a detailed scenario for the degradation of $MAPbI_3$ crystals in a mixture of O_2 and H_2O. In the present AIMD simulation, the observed intermolecular interactions are completely different from those in the case in which only O_2 or H_2O exists.[24] In the initial state, the O_2 molecule is easily adsorbed near the I^- anion at the surface of $MAPbI_3$ irrespective of the charge state (see filled square line 0–80 fs of Fig. 4e), and it attempts to directly interact with Pb atoms (see 0–180 fs of Fig. 4d). However, different interplays of H_2O and O_2 molecules with $MAPbI_3$ components occur depending on the charge state (see Fig. 4e and f). In the case of a +1-charge state (one localized hole), the I–O interaction stabilizes (blue-filled square line in Fig. 4e) and the H_2O molecule approaches the I–O (blue-filled square line in Fig. 4f). As the positive charge of the Pb atom is

partially increased by a localized hole in the $MAPbI_3$ slab, the Pb–O bond is finally formed after 500 fs (see Fig. 4d). An H_2O molecule could then provide a proton to the Pb-bonded O atom, which is followed by the formation of stable hydroxide species (Pb–I–O–OH) (see blue filled square line in Fig. 4f). At the same time, the MA cation is completely deprotonated owing to the donation of a proton to deprotonated H_2O (OH^-) (Fig. 4f). We studied time evolution of the Bader charge of Pb, I, O, O and H atoms for the whole simulation (see ESI Table 3†). It was observed that electrons transferred to O atoms, which is indicative of strong Pb–O and O–H interactions. Consequently, such generation of hydroxide species and deprotonation of MA cations cause the rapid destruction of a $MAPbI_3$ unit cell. The prediction of the formation of Pb–I–O–OH is experimentally evidenced (see below).

In the case of the −1-charge state (one localized electron), the I–O interaction abruptly weakens after 100 fs, as shown in Fig. 4e, which is probably due to the augmented negative charge of I atoms. Subsequently, the Pb–O interaction is not strengthened sufficiently to form a stable Pb–O bond (see red line of Fig. 4d), and the H_2O molecule then separates from the adsorbed O_2 molecule, which is indicative of the lack of proton transfer (see red square line at approximately 500–600 fs in Fig. 4f). In this case, the PbI_6^- octahedron is stabilized owing to the absence of proton transfer. In the neutral charge state case (no localized charge), no intermolecular interaction between the gas molecules and components of $MAPbI_3$ occurs, which means that no degradation of the $MAPbI_3$ crystal occurs, as expected (see Fig. 4b and black lines of Fig. 4d–f). In summary, the vigorous decomposition of

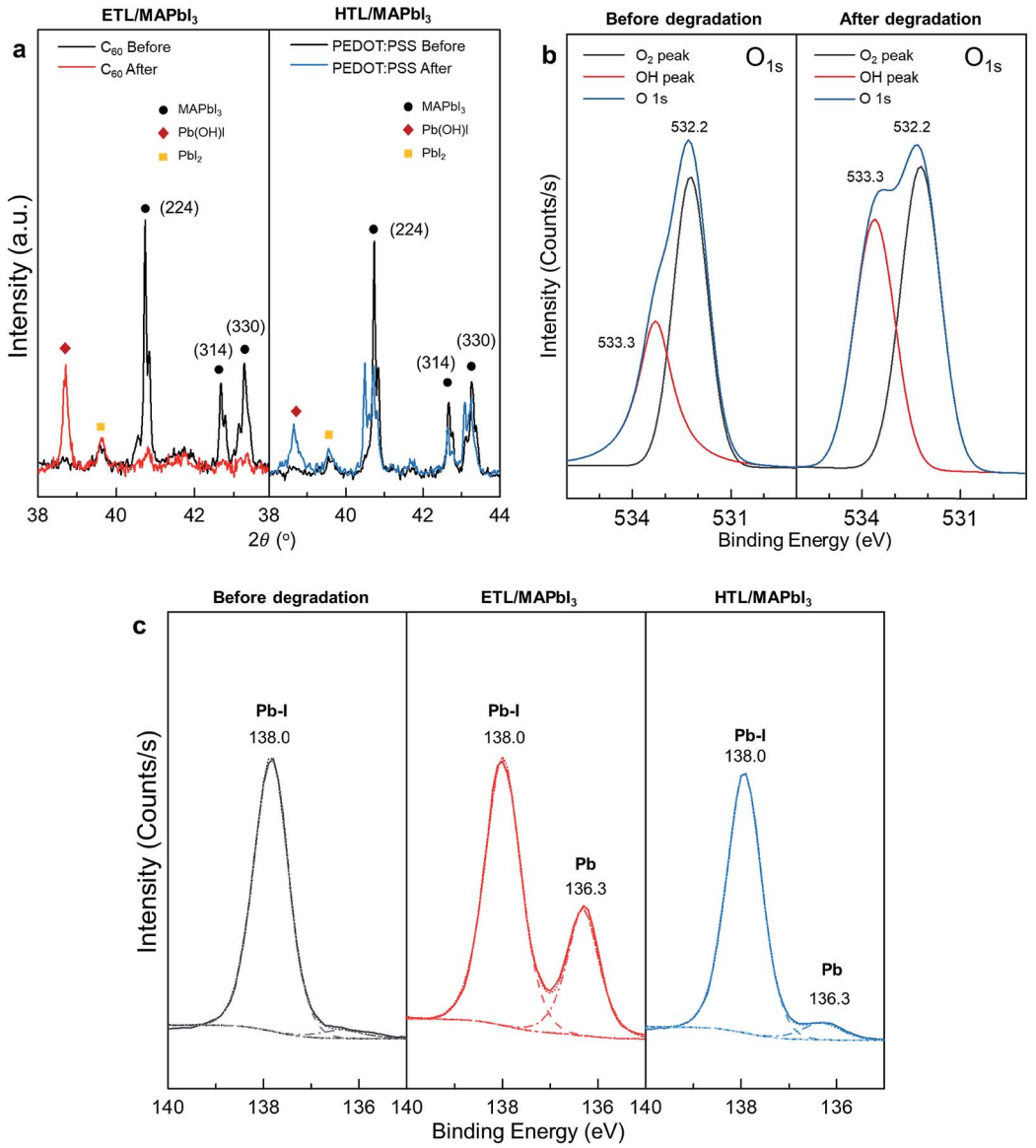

Fig. 5 Observation of hydroxide species and metallic Pb as the result of light-induced perovskite film degradation. (a) XRD patterns of degraded $MAPbI_3$ films deposited on the ETL and HTL in the range between 38° to 44° 2θ. $MAPbI_3$, Pb(OH)I and PbI_2 peaks are indexed. (b) XPS spectra recorded for the O atom (O 1s) of the ETL/$MAPbI_3$ film before and after degradation. (c) XPS spectra recorded for the Pb atom (Pb $4f_{7/2}$) of the fresh, ETL/$MAPbI_3$ and HTL/$MAPbI_3$ samples.

$MAPbI_3$ crystals occurs in an environment of a mixture of O_2 and H_2O through deprotonation with localized holes.

X-ray-assisted spectroscopic results supporting degradation scenario

To obtain experimental evidence of our degradation scenario, we measured and analyzed X-ray-assisted spectroscopy data of fresh and degraded $MAPbI_3$ samples. First, we detected solid Pb(OH)I as one of the lead hydroxide products appearing at 38.7° in the XRD patterns of the degraded $MAPbI_3$ films in Fig. 5a.[38] These results agree with the generation of lead hydroxide species in our AIMD simulation in the environment of the O_2 and H_2O mixture. The existence of hydroxide was also observed from the comparison of the X-ray photoelectron spectroscopy (XPS) data for the fresh and degraded $MAPbI_3$ film. As shown in Fig. 5b, the O 1s peak shifts to the higher binding energy region for the degraded sample, which means that the O–H bonding character is reinforced.[39–41] In other words, hydroxide species are produced as an end product of the degradation, as we hypothesized previously. The XPS spectra highlight another piece of crucial evidence in terms of iodine loss. Fig. 5c shows the XPS spectra of the fresh $MAPbI_3$, degraded ETL/$MAPbI_3$, and degraded HTL/$MAPbI_3$ within the range from 135 eV to 140 eV. In the fresh sample, only a Pb–I bond is detected, as identified from the Pb $4f_{7/2}$ peak appearing at 138.0 eV. After the degradation, the distinct peak of 136.3 eV corresponding to metallic Pb appears in both cases of the ETL/$MAPbI_3$ and HTL/$MAPbI_3$ sample, which is indicative of iodine loss, *i.e.*, the complete destruction of the PbI_6^- octahedra.[42–44] The peak intensity of the ETL/$MAPbI_3$ is much higher than that of the HTL/$MAPbI_3$, which is consistent with our simulation results, in that the $MAPbI_3$ crystal is more unstable at the +1-charge state as compared to the −1-charge state.

Conclusions

We report different light-induced degradation rates of $MAPbI_3$ films depending on the charge polarity selectivity of the underlying transporting layer under various surrounding ambient conditions. It was confirmed that localized carrier polarities occurred in the $MAPbI_3$ film as the charge selectivity of the underlying layer plays a decisive role in determining the degradation rate of the $MAPbI_3$ films. The $MAPbI_3$ films with localized holes were more rapidly degraded in the presence of H_2O than the ones with localized electrons, whereas an inverted trend of the degradation rate appeared under O_2-only ambient conditions. Interestingly, the combination of H_2O and O_2 resulted in the fastest degradation for the localized hole-rich $MAPbI_3$ film, while the $MAPbI_3$ film with localized electrons was unexpectedly stabilized in contrast to the case of the O_2-only condition. To explain these observations, we investigated the intermolecular dynamics of H_2O, O_2, and the components of $MAPbI_3$ for different charge states through DFT-based AIMD simulations. The dramatic difference in the degradation rates under mixed atmosphere conditions is mainly attributed to the formation of strong Pb–O interactions and the subsequent generation of lead hydroxide species for $MAPbI_3$ crystals with localized holes, which was evidenced by the XPS and XRD results. Our study suggests that the positive localized charge in the $MAPbI_3$ crystals drives fast de-crystallization under actual atmospheric conditions and, thus, provides the future direction for the secure long-term stability of perovskite solar cells.

Methods

Materials and device fabrication

All the materials were used as received. The ITO glass substrates (AMG, 9.5 Ω cm^{-2}) were cleaned by sonication in acetone, isopropanol, and deionized water followed by the deposition of the transporting materials. A 35 nm thick C_{60} layer was coated onto the ITO glass substrate using a vacuum thermal evaporator at a deposition rate of 0.2 Å s^{-1} and pressure of 10^{-7} torr. A single 6,6-phenyl-C61-butyric acid methyl ester ($PC_{60}BM$) layer was spin-coated at a rotation speed of 2000 rpm for 60 s using its 10 mg mL^{-1} solution in chlorobenzene (Sigma-Aldrich Corporation) and then annealed at a temperature of 100 °C for 10 min. A Spiro-MeOTAD (Merck) layer was drop-cast on a spinning substrate at a rotation speed of 3000 rpm for 30 s using its 72.3 mg mL^{-1} solution in chlorobenzene. A PEDOT:PSS (Clevios, AI4083) layer was spin-coated at a speed of 5000 rpm for 40 s using its 1 : 1 (v/v) diluted solution in deionized water and then annealed at 130 °C for a minimum of 30 min. $MAPbI_3$ perovskite solutions were prepared by mixing PbI_2 (Alfa Aesar), MAI (Xi'an Chemical), dimethyl sulfoxide (DMSO, Sigma-Aldrich), and dimethylformamide (DMF, Sigma-Aldrich) in specified proportions. For example, to prepare 52 wt% precursor in a DMF solvent with the molecular ratio of PbI_2 : MAI : DMSO = 1 : 1 : 1, 461 mg of PbI_2, 159 mg of MAI, and 78 mg of dimethyl sulfoxide were mixed in 0.60 mL of DMF. After spin-coating the obtained precursor at a speed of 4000 rpm for 20 s and performing a diethyl ether dripping procedure, the resulting intermediate films were annealed at 100 °C for 10 min. All the spin-coating procedures in this study were performed in a dry room with a relative humidity of less than 10% and temperature of 25 °C.

Ageing conditions

All the perovskite films were exposed to light in a controlled environment using a customized chamber. Dry-air conditions were configured by supplying dry air (80% nitrogen/20% oxygen) at 0.5 L m^{-1}. The H_2O conditions were configured by supplying nitrogen gas with an H_2O bubbler at 0.5 L m^{-1}. The mixed ambient conditions were configured by supplying dry air with an H_2O bubbler at 0.5 L m^{-1}. Light illumination was performed under 1-sun conditions using an AAA solar simulator (Newport Oriel Solar 3A Class AAA, 64023A). The light intensity was calibrated using a KG-5 standard silicon solar cell (Oriel, VLSI Standards).

Characterization

Time-resolved and steady-state PL measurements were conducted using a FluoroMax-4 spectrofluorometer (Horiba). The studied films were photo-excited with a 463 nm laser diode (DeltaDiode-470L, Horiba) pulsed at a frequency of 100 MHz.

The resulting PL was detected using a high-sensitivity photon-counting near infrared (NIR) detector. Cross-sectional scanning electron microscopic (SEM) images of the perovskite solar cell structure were obtained using a field-emission SEM (FESEM, AURIGA, Carl Zeiss) combined with a focused ion beam system (FIB system, AURIGA, Carl Zeiss). The absorbance spectra and crystalline diffraction patterns were recorded using an ultraviolet-visible/NIR spectrophotometer (Cary 5000, Agilent Technologies) and an X-ray diffractometer (New D8 Advance, Bruker), respectively. The XPS spectra were obtained using an electron spectroscopy instrument for chemical analysis (Sigma Probe, VG Systems). Scanning Kelvin Probe Microscopy (SKPM) measurements were performed in non-contact mode using an atomic force microscope (NX10, Park Systems) equipped with an NSC36/Cr–Au tip.

DFT calculation

The conditions for the DFT calculation and unit cell preparations were almost identical to those in our previous work.[24] All the calculations were performed using the Vienna Ab initio Simulation Package (VASP, version 5.3.5),[45] and the atomic geometries were visualized using VESTA (Visualization for Electronic and STructural Analysis) and the VMD (Visual Molecular Dynamics) program.[46,47] The projector augmented wave method[48,49] was applied to describe the electron-ion interactions with an energy cutoff of 520.0 eV for the plane waves. The Perdew–Burke–Ernzerhof exchange–correlation functional[50] was used, and the weak van der Waals interactions were also considered using the zero damping DFT-D3 method of Grimme.[51] Spin-polarized calculations were performed to reflect the triplet nature of an oxygen molecule, and the Brillouin-zone was sampled with a Γ-centered $(4 \times 1 \times 4)$ Monkhorst-Pack k-point grid for structural relaxation and a single Γ-point for the AIMD simulations. All the AIMD simulations were performed in the canonical ensemble using a Nosé-Hoover thermostat with a temperature of 298 K and a 1 fs time-step. The primary unit cell was prepared by placing water and oxygen molecules ($3H_2O$ and $1O_2$ or $2H_2O$ and $1O_2$) near the surface PbI_6^- octahedron of the perovskite crystal comprising four $MAPbI_3$ units, which is reproduced based on the experimentally proven crystal structure[52] with a slight modification, as previously used.[24] We confirmed that there was no significant effect of simulation size by performing calculations for a 2×1 supercell ($8H_2O$ units).[24] The initial unit cell geometries for the AIMD simulations were completed by relaxing the water molecules, oxygen molecule, and two upper $MAPbI_3$ units to a neutral state. In all the relaxations and simulations, the two $MAPbI_3$ units at the bottom were fixed while all the other atoms that comprise water, oxygen, and the $MAPbI_3$ units at the top were allowed to move. We showed the simulation for 1 picosecond because main reactions actively happened in the initial state. ESI Fig. 12† shows simulation results for 1.5 picoseconds.

Conflicts of interest

There are no conflicts to declare.

Acknowledgements

This work was supported by the Global Frontier R&D Program of the Center for Multiscale Energy Systems funded by the National Research Foundation under the Ministry of Science and ICT, Korea (2012M3A6A7054855). This work was also supported by the National Research Foundation under the Ministry of Science and ICT, Korea (2017R1A2B3010927). The XRD patterns were measured at the Research Institute of Advanced Materials at Seoul National University. This research was supported by Creative Materials Discovery Program through the National Research Foundation of Korea (NRF) funded by Ministry of Science and ICT(2016M3D1A1027664).

References

1 N. Ahn, D.-Y. Son, I.-H. Jang, S. M. Kang, M. Choi and N.-G. Park, *J. Am. Chem. Soc.*, 2015, **137**, 8696–8699.
2 H. S. Kim, C. R. Lee, J. H. Im, K. B. Lee, T. Moehl, A. Marchioro, S. J. Moon, R. Humphry-Baker, J. H. Yum, J. E. Moser, M. Gratzel and N. G. Park, *Sci. Rep.*, 2012, **2**, 591.
3 A. Kojima, K. Teshima, Y. Shirai and T. Miyasaka, *J. Am. Chem. Soc.*, 2009, **131**, 6050–6051.
4 W. S. Yang, B.-W. Park, E. H. Jung, N. J. Jeon, Y. C. Kim, D. U. Lee, S. S. Shin, J. Seo, E. K. Kim and J. H. Noh, *Science*, 2017, **356**, 1376–1379.
5 D. Bryant, N. Aristidou, S. Pont, I. Sanchez-Molina, T. Chotchunangatchaval, S. Wheeler, J. R. Durrant and S. A. Haque, *Energy Environ. Sci.*, 2016, **9**, 1655–1660.
6 J. A. Christians, P. A. Miranda Herrera and P. V. Kamat, *J. Am. Chem. Soc.*, 2015, **137**, 1530–1538.
7 J.-H. Lee, N. C. Bristowe, P. D. Bristowe and A. K. Cheetham, *Chem. Commun.*, 2015, **51**, 6434–6437.
8 I. A. Shkrob and T. W. Marin, *J. Phys. Chem. Lett.*, 2014, **5**, 1066–1071.
9 Z. Zhu, V. G. Hadjiev, Y. Rong, R. Guo, B. Cao, Z. Tang, F. Qin, Y. Li, Y. Wang and F. Hao, *Chem. Mater.*, 2016, **28**, 7385–7393.
10 G. Niu, X. Guo and L. Wang, *J. Mater. Chem. A*, 2015, **3**, 8970–8980.
11 N. Aristidou, I. Sanchez-Molina, T. Chotchuangchutchaval, M. Brown, L. Martinez, T. Rath and S. A. Haque, *Angew. Chem., Int. Ed.*, 2015, **54**, 8208–8212.
12 G. Divitini, S. Cacovich, F. Matteocci, L. Cina, A. Di Carlo and C. Ducati, *Nat. Energy*, 2016, **1**, 15012.
13 A. Guerrero, J. You, C. Aranda, Y. S. Kang, G. Garcia-Belmonte, H. Zhou, J. Bisquert and Y. Yang, *ACS Nano*, 2015, **10**, 218–224.
14 Y. Han, S. Meyer, Y. Dkhissi, K. Weber, J. M. Pringle, U. Bach, L. Spiccia and Y.-B. Cheng, *J. Mater. Chem. A*, 2015, **3**, 8139–8147.
15 T. A. Berhe, W.-N. Su, C.-H. Chen, C.-J. Pan, J.-H. Cheng, H.-M. Chen, M.-C. Tsai, L.-Y. Chen, A. A. Dubale and B.-J. Hwang, *Energy Environ. Sci.*, 2016, **9**, 323–356.
16 S. Yang, W. Fu, Z. Zhang, H. Chen and C.-Z. Li, *J. Mater. Chem. A*, 2017, **5**, 11462–11482.

17 T. Leijtens, E. T. Hoke, G. Grancini, D. J. Slotcavage, G. E. Eperon, J. M. Ball, M. De Bastiani, A. R. Bowring, N. Martino, K. Wojciechowski, M. D. McGehee, H. J. Snaith and A. Petrozza, *Adv. Energy Mater.*, 2015, **5**, 1500962.
18 S. Bae, S. Kim, S.-W. Lee, K. J. Cho, S. Park, S. Lee, Y. Kang, H.-S. Lee and D. Kim, *J. Phys. Chem. Lett.*, 2016, **7**, 3091–3096.
19 N. Aristidou, C. Eames, M. S. Islam and S. A. Haque, *J. Mater. Chem. A*, 2017, **5**, 25469–25475.
20 R. Brenes, C. Eames, V. Bulovic, M. S. Islam and S. D. Stranks, *Adv. Mater.*, 2018, **30**, e1706208.
21 B. Charles, J. Dillon, O. J. Weber, M. S. Islam and M. T. Weller, *J. Mater. Chem. A*, 2017, **5**, 22495–22499.
22 N. Aristidou, C. Eames, I. Sanchez-Molina, X. Bu, J. Kosco, M. S. Islam and S. A. Haque, *Nat. Commun.*, 2017, **8**, 15218.
23 N. Ahn, K. Kwak, M. S. Jang, H. Yoon, B. Y. Lee, J.-K. Lee, P. V. Pikhitsa, J. Byun and M. Choi, *Nat. Commun.*, 2016, **7**, 13422.
24 K. Kwak, E. Lim, N. Ahn, J. Heo, K. Bang, S. K. Kim and M. Choi, 2017, arXiv preprint arXiv:1709.04130.
25 M.-C. Kim, Y. U. Jin, B. J. Kim, D. Lee, H. S. Jung and M. Choi, *MRS 2017 Fall Meeting*, Boston, USA, 2017.
26 M.-C. Kim, PhD Engineering Doctorate, Seoul National University, 2018.
27 E. M. Hutter, J.-J. Hofman, M. L. Petrus, M. Moes, R. D. Abellón, P. Docampo and T. J. Savenije, *Adv. Energy Mater.*, 2017, 1602349, DOI: 10.1002/aenm.201602349.
28 K. Wojciechowski, T. Leijtens, S. Siprova, C. Schlueter, M. T. Hörantner, J. T.-W. Wang, C.-Z. Li, A. K.-Y. Jen, T.-L. Lee and H. J. Snaith, *J. Phys. Chem. Lett.*, 2015, **6**, 2399–2405.
29 J. Seo, S. Park, Y. C. Kim, N. J. Jeon, J. H. Noh, S. C. Yoon and S. I. Seok, *Energy Environ. Sci.*, 2014, **7**, 2642–2646.
30 J. H. Heo, H. J. Han, D. Kim, T. K. Ahn and S. H. Im, *Energy Environ. Sci.*, 2015, **8**, 1602–1608.
31 M. Saliba, T. Matsui, J.-Y. Seo, K. Domanski, J.-P. Correa-Baena, M. K. Nazeeruddin, S. M. Zakeeruddin, W. Tress, A. Abate and A. Hagfeldt, *Energy Environ. Sci.*, 2016, **9**, 1989–1997.
32 S. D. Stranks, V. M. Burlakov, T. Leijtens, J. M. Ball, A. Goriely and H. J. Snaith, *Phys. Rev. Appl.*, 2014, **2**, 034007.
33 H. Greijer, J. Lindgren and A. Hagfeldt, *J. Phys. Chem. B*, 2001, **105**, 6314–6320.
34 J. Liu, Y. Wu, C. Qin, X. Yang, T. Yasuda, A. Islam, K. Zhang, W. Peng, W. Chen and L. Han, *Energy Environ. Sci.*, 2014, **7**, 2963–2967.
35 P. Zhao, W. Yin, M. Kim, M. Han, Y. J. Song, T. K. Ahn and H. S. Jung, *J. Mater. Chem. A*, 2017, **5**, 7905–7911.
36 C. Motta, F. El-Mellouhi and S. Sanvito, *Sci. Rep.*, 2015, **5**, 12746.
37 F. Mohn, L. Gross, N. Moll and G. Meyer, *Nat. Nanotechnol.*, 2012, **7**, 227–231.
38 A. Babayigit, D. D. Thanh, A. Ethirajan, J. Manca, M. Muller, H.-G. Boyen and B. Conings, *Sci. Rep.*, 2016, **6**, 18721.
39 K.-H. Jung, J.-Y. Seo, S. Lee, H. Shin and N.-G. Park, *J. Mater. Chem. A*, 2017, **5**, 24790–24803.
40 H. L. Mosbacker, Y. M. Strzhemechny, B. D. White, P. E. Smith, D. C. Look, D. C. Reynolds, C. W. Litton and L. J. Brillson, *Appl. Phys. Lett.*, 2005, **87**, 012102.
41 M. M. Sabri, J. Jung, D. H. Yoon, S. Yoon, Y. J. Tak and H. J. Kim, *J. Mater. Chem. C*, 2015, **3**, 7499–7505.
42 B. Conings, J. Drijkoningen, N. Gauquelin, A. Babayigit, J. D'Haen, L. D'Olieslaeger, A. Ethirajan, J. Verbeeck, J. Manca and E. Mosconi, *Adv. Energy Mater.*, 2015, **5**, 1500477.
43 G. R. Kumar, A. D. Savariraj, S. Karthick, S. Selvam, B. Balamuralitharan, H.-J. Kim, K. K. Viswanathan, M. Vijaykumar and K. Prabakar, *Phys. Chem. Chem. Phys.*, 2016, **18**, 7284–7292.
44 T.-W. Ng, C.-Y. Chan, M.-F. Lo, Z. Q. Guan and C.-S. Lee, *J. Mater. Chem. A*, 2015, **3**, 9081–9085.
45 J. Hafner, *J. Comput. Chem.*, 2008, **29**, 2044–2078.
46 W. Humphrey, A. Dalke and K. Schulten, *J. Mol. Graphics*, 1996, **14**, 33–38.
47 K. Momma and F. Izumi, *J. Appl. Crystallogr.*, 2011, **44**, 1272–1276.
48 P. E. Blöchl, *Phys. Rev. B: Condens. Matter Mater. Phys.*, 1994, **50**, 17953–17979.
49 G. Kresse and D. Joubert, *Phys. Rev. B: Condens. Matter Mater. Phys.*, 1999, **59**, 1758–1775.
50 J. P. Perdew, K. Burke and M. Ernzerhof, *Phys. Rev. Lett.*, 1996, **77**, 3865–3868.
51 G. Stefan, A. Jens, E. Stephan and K. Helge, *J. Chem. Phys.*, 2010, **132**, 154104.
52 T. Baikie, Y. Fang, J. M. Kadro, M. Schreyer, F. Wei, S. G. Mhaisalkar, M. Graetzel and T. J. White, *J. Mater. Chem. A*, 2013, **1**, 5628–5641.